ADVANCES IN ATMOSPHERIC SCIENCES, VOL. 30, NO. 2, 2013, 263–279

A Study on a Snowband Associated with a Coastal Front and Cold-Air Damming Event of 3–4 February 1998 along the Eastern Coast of the Korean Peninsula

Jae-Gyoo LEE[1] and Ming XUE*[2,3]

[1]*Department of Atmospheric Environmental Sciences Kangnung National University, Kangnung, Korea*

[2]*Center for Analysis and Prediction of Storms, Norman OK, USA*

[3]*School of Meteorology, University of Oklahoma, Norman OK, USA*

(Received 28 April 2012; revised 1 August 2012)

ABSTRACT

A 24-h simulation with the Advanced Regional Prediction System (ARPS) nonhydrostatic model is performed for the heavy snowfall event of 3–4 February 1998 along the eastern coast of Korean Peninsula; the results are used to understand the snowfall process, including why the precipitation maxima formed along the Yeongdong coastal region rather than over the mountain slope and ridge top during.

The numerical simulation with a 4-km horizontal grid spacing and 43 levels reproduces very well the narrow snowband located off the eastern Korean coast, away from, instead of over, the Yeongdong coastal mountain range. The general evolution of the snowband agrees quite well with radar observations, while the water-equivalent precipitation amount agrees reasonably well with radar precipitation estimate. The simulation results clearly show that the snow band developed due to the lifting by a coastal front that developed because of the damming of cold air against the eastern slope of the coastal mountain range. The damming was enhanced by the advection of cold air by a low-level mountain-parallel jet from the north, formed due to geostrophic adjustment as the on-shore upslope air was decelerated by the mountain blocking. As the onshore flow weakened later due to synoptic-scale flow pattern change, the cold front propagated off shore and the precipitation dissipated.

Key words: coastal snowfall, cold air damming, orographic precipitation

Citation: Lee, J.-G., and M. Xue, 2013: A study on a snowband associated with a coastal front and cold-air damming event of 3–4 February 1998 along the eastern coast of the Korean Peninsula. *Adv. Atmos. Sci.*, **30**(2), 263–279, doi: 10.1007/s00376-012-2088-6.

1. Introduction

When cold northerly or northeasterly winds blow from a well developed Siberian High over the East Sea (see Fig. 1), the cold air mass crossing the sea becomes modified by the rich heat and moisture fluxes from the warm sea surface below, resulting in instability and convection in the boundary layer (e.g., Ninomiya, 1968; Jhun et al., 1994). Furthermore, if the winds over the sea are relatively strong and persistent, the convection can organize into snowbands, leading to the heavy snowfall on the windward (East Sea facing) side of the Korean Peninsula and the Japan Islands (Nagata et al., 1986; Seo and Jhun, 1991; Lee and Lee, 1994). This often leads to heavy snowfall over short periods of time in the absence of a synoptic scale trough or low system. Thus, forecasters need to pay close attention to the development of such Siberian high-pressure systems.

Related to the combined effects of orography and ocean on snowfall in the eastern Asian region, Estoque and Ninomiya (1976) performed a numerical study on snowfall distribution associated with the East Sea; they showed that for their case the occurrence of snowfall was controlled primarily by orographic lifting. The snowfall on the windward side of the Korean Peninsula and the Japan Islands is similar to the ocean-effect snow which has been observed near the New Eng-

*Corresponding author: Ming XUE, mxue@ou.edu

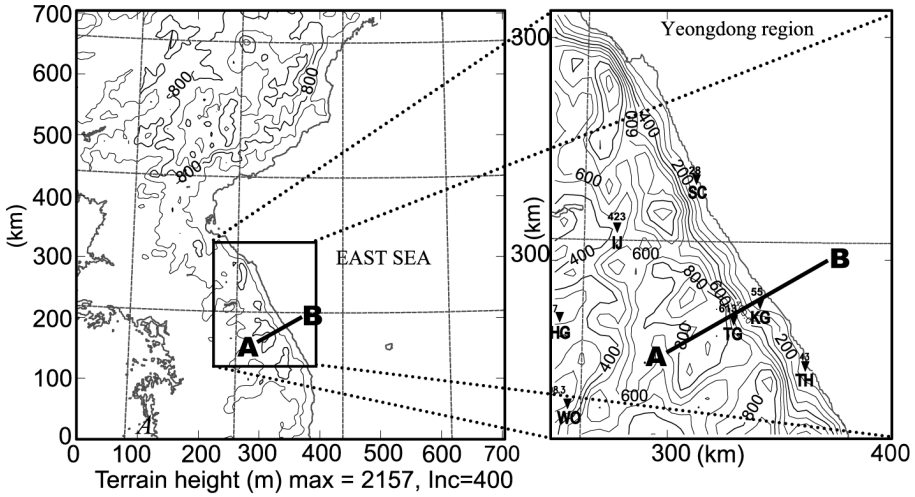

Fig. 1. The 4-km-resolution ARPS simulation domain with topography contours at 400-m intervals (left) and a smaller sub-doamin with more detailed orography at 100-m intervals (right). The subdomain corresponding to the rectangular box in the left panel indicates the Yeongdong region which is the focus region for the study. Solid line A-B indicates the location of the cross sections shown in later figures, which is roughly normal to the axis of the costal mountains passing through Kangnung. The locations marked by black inverse triangles include surface observation sites SC (Sokcho), KG (Kangnung), TG (Taegwallyong), and radar site TH (Tonghae). The numbers above the triangles indicate the height of the sites above sea level.

land coast of the United States (Waldstreicher, 2002). Such snowfall is also similar to the "lake-effect snow" of the Great Lakes (e.g., Eichenlaub, 1979; Hjelmfelt and Braham, 1983; Niziol et al., 1995) of North America, where the underlying warm water provides a large amount of heat and moist that feeds the snowfall. During cold air outbreaks, the coast line shape and sea surface temperature pattern have profound effects on the establishment of low-level mesoscale circulations as a result of differential heating that is dependent on both over-water fetch and water temperature (Atlas et al., 1983).

For the Korean Peninsula, when cold northeasterly winds persist, the Yeongdong region, the main windward side of the Korean Peninsula, is subject to heavy snowfall. Thus, heavy snowfall forecasting in the Yeongdong region is of primary concern during the winter season. Figure 1 shows the topography of the Korean Peninsula and that of the Yeongdong region in a simulation domain of the Advanced Regional Prediction System (ARPS, Xue et al., 2000, 2001, 2003) that is used in this study. The Yeongdong region consists of narrow and steep mountains (called the Taebaek Mountains) with an average height of about 1 km. The mountain range is asymmetric with its steeper slope facing the eastern coast, and there exists a narrow coastal plain region of about 5 km wide between the mountains and the coast. The axis of the mountain range runs approximately northwest to southeast, roughly parallel to the coastline. With such geographical and topographical conditions, the snowfall distribution in this region can be rather complicated because of the combined effects of ocean and topography. For these reasons, the Yeongdong region has drawn much interest of researchers.

The topography of the Yeongdong region may also be favorable for cold-air damming, which often occurs in the eastern United States in the winter. In the latter region, cold, stable air from a surface high over New England or southeastern Canada flows southwestward and is channeled along the eastern slopes of the Appalachians. The mountains "dam" the air along the eastern slopes (Richwien, 1980; Forbes et al., 1987; Bell and Bosart, 1988; Stauffer and Warner, 1987). Furthermore, the cold-air advection associated with the damming intensifies the thermal contrast between the dammed air and that over the ocean, which has been warmed and moistened by the underlying sea (Sanders and Gyakum, 1980; Bosart, 1981). This process enhances the baroclinic zone near the coastline, causing coastal frontogenesis (Bosart, 1975; Forbes et al., 1987; Stauffer and Warner, 1987), and such frontogenesis is usually restricted to the lower atmosphere.

If it were purely orographic lifting, the heaviest precipitation is expected near the slope of and/or over the ridge of the mountains. Observations in the Yeong-

dong region, however, often show that the maximum precipitation is located over the coastal plain. According to Lee (1999), among the 159 days from January 1978 through February 1988 on which 24-h accumulated snowfall depth exceeded 10 cm, on 19% of the days, the snowfall amount in the coastal exceeded that over the mountain areas while on 48% of the days, the amounts over the two regions were comparable. This indicates that on a majority of the days snowfall started over the coastal regions rather than over the windward slope. Cold-air damming and associated coastal front are suspected to have caused such a displacement.

Modeling and diagnostic studies on the causes of winter snowfall in the windward coastal region of Korea had not been carried out until very recently. Lee and Kim (2008) reported on the results of a numerical simulation of a heavy snowfall event that occurred 13 January 2008 along the Yeongdong coastal area, obtained using the Weather Research and Forecasting (WRF) model (Skamarock et al., 2005). The results suggested the important role of cold air damming along the east side of the coastal mountains. In Lee et al. (2011), air flow trajectory analyses were further performed on the simulation data of the 13 January 2008 case, and upward motion was found to be located off the mountain slope along a coastal front, confirming the earlier suggestions.

In this paper, we report on the results of a modeling study on another snowfall event that occurred in the Yeongdong coastal region, i.e., the event of 3–4 February 1998. On that day, snowfall maxima were also observed along the Yeongdong coastal region rather than over the mountain slope and ridge top. We again try to understand the processes in this event by examining available observations and by performing a numerical simulation.

The respect of this paper is organized as follows. In section 2, observational analyses are first presented; surface weather maps, the distribution of accumulated snowfall, satellite imagery, radar reflectivity, and surface wind observations are examined. A description of the numerical model and simulation is given in section 3 while the simulation results are discussed in section 4. Summary and conclusions are given in section 5.

2. Observational analysis

Figure 2 shows the surface weather charts at 1200 UTC (2100 LST) 3 February (Fig. 2a) and at 1200 UTC 4 February 1998 (Fig. 2b). In Fig. 2a, a well-developed Siberian High, centered near Mongolia at 1200 UTC 3 February 1998, 2–3 hours before the start of Korean coastal snowfall, dominated most of China. A ridge extended eastward from the High over the East Sea. On the downwind or south side of the ridge, northeasterly, quasi-geostrophic winds of cold air blew over the warm sea surface. In particular, over the northern part of East Sea, horizontal pressure gradient was relatively strong and the isotherms were nearly perpendicular to the isobars (not shown), indicating strong cold advection over the sea and in the eastern coastal region of Korea. As this continental polar air mass was advected over the warm sea surface, it was rapidly modified by the large oceanic heat and moisture fluxes (as is evidenced by the development of cloud streets over the ocean in Fig. 3), leading to an increase in convective instability that also occurs in lake-effect snow cases. This rendered a favorable condition for forming convective snow clouds, especially in the downwind fetch of the flow. Furthermore, northeasterly, quasi-geostrophic winds normal to the axis of the mountains was favorable for cold-air damming on the eastern side of the Taebaek mountains. The associated mesoscale features are, however, often difficult to identify from synoptic charts.

Figure 2b shows the surface weather chart at 1200 UTC 4 February, about eight hours after the coastal snowfall ended. By this time, the alignment of isobars over the central and northern part of the East Sea had been changed from the northeast-southwest to northwest-southeast orientation, hence the geostrophic winds in the region backed to northwesterly, more or less parallel to the coastal mountain range. Such winds are unfavorable for cold-air damming and would cause the weakening of temperature contrast in the coastal region also.

The distribution of 24-h accumulated snowfall depth ending at 1500 UTC (2400 LST) 4 February 1998 is shown in Fig. 4 (more frequent snow depth data are not available). Toward the mountainous inland regions, the snowfall decreased rapidly. The area of maximum snowfall was located near and off the coast rather than further inland over the mountain slope. That is, a significant amount of snowfall was located along the coastal plain region (e.g., 16.0 cm at Kangnung, KG in Fig. 4) rather than over the mountain region (e.g., 6.3 cm over Taegwallyong, TG in Fig. 4) where the orographic lifting is strong. The National Oceanic and Atmospheric Administration (NOAA) infrared satellite images of the 10.5–11.5 μm channel at 1751 and 2132 UTC 3 February 1998, when the snowfall at Kangnung was active, are shown in Fig. 3. The main cloud band was clearly aligned along the coastline, parallel to the axis of the mountains, but the central axis of the band was located somewhat off the coast line over the sea.

More detailed structures and evolution of the pre-

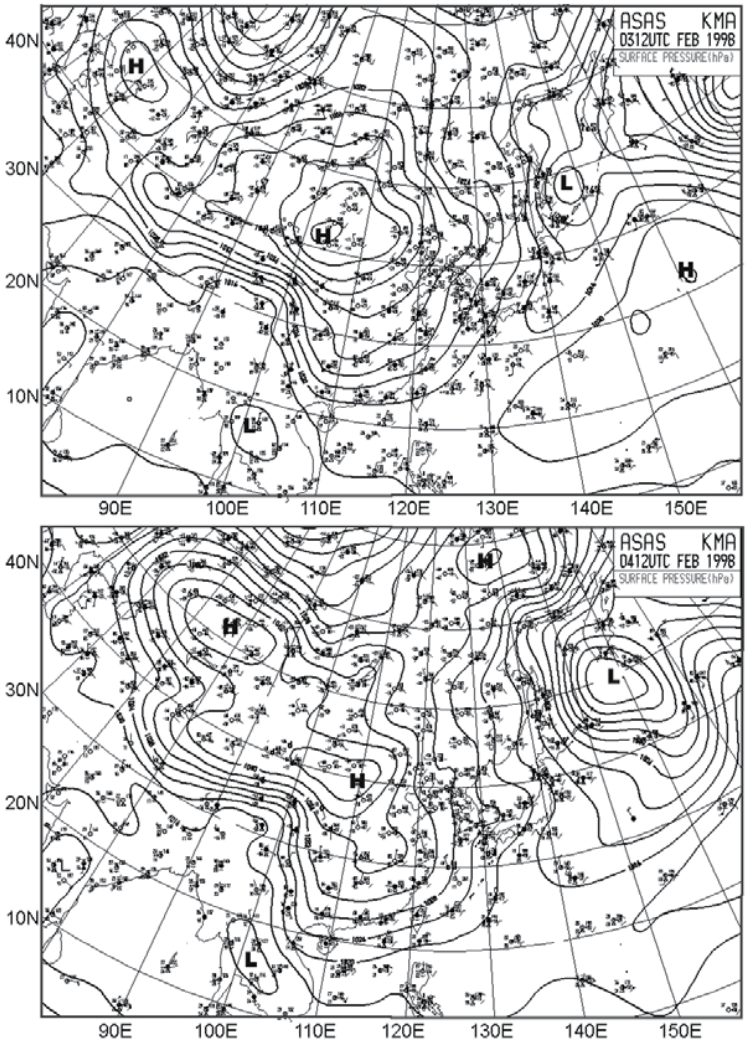

Fig. 2. Synoptic surface weather charts at (a) 1200 UTC 3 February and (b) at 1200 UTC 4 February 1998.

cipitation can be seen from the base reflectivity maps, presented in terms of the estimated precipitation rate, from an operational radar located at Tonghae (Fig. 5). Precipitation rates up to 4 mm h^{-1} (level two of gray shading) are found within these images. At 1200 UTC (not shown), no precipitation echoed was observed. An elongated precipitation region, aligned more or less along but mostly off the coast, has already developed by 1300 UTC (Fig. 5a) and evolved into a more banded structure and gained a larger level-2 precipitation core (1–4 mm h^{-1}) by 1500 UTC (Fig. 5b). By 1800 UTC, the precipitation band became narrower and the level-2 core shrank somewhat (Fig. 5c) and the precipitation pattern stayed essentially the same by 2100 UTC (Fig. 5d). By 0000 UTC (Fig. e), the level-2 precipitation core essentially disappeared and by 0300 UTC, the first level of precipitation (0–1 mm h^{-1}) was disappearing. Within the next hour, the precipitation completely dissipated (not shown). In general, the precipitation band is centered 10–20 km off the coastline. This long, narrow, banded structure suggests the existence of a coastal front.

Figure 6 shows the observed surface winds at 1800 UTC 3 February 1998. Northwesterly, cross-isobaric winds (due to frictional effects and terrain blocking, etc., c.f., Fig. 2) prevailed at this time over land and along the Yeongdong coastal region, except at Kangnung which had very weak southwesterly winds (which may be due to local orographic and/or snowfall effects). Meanwhile, northeasterly winds, which are in the direction of geostrophic winds, were observed at the island of Ullungdo far off the east coast. This rep-

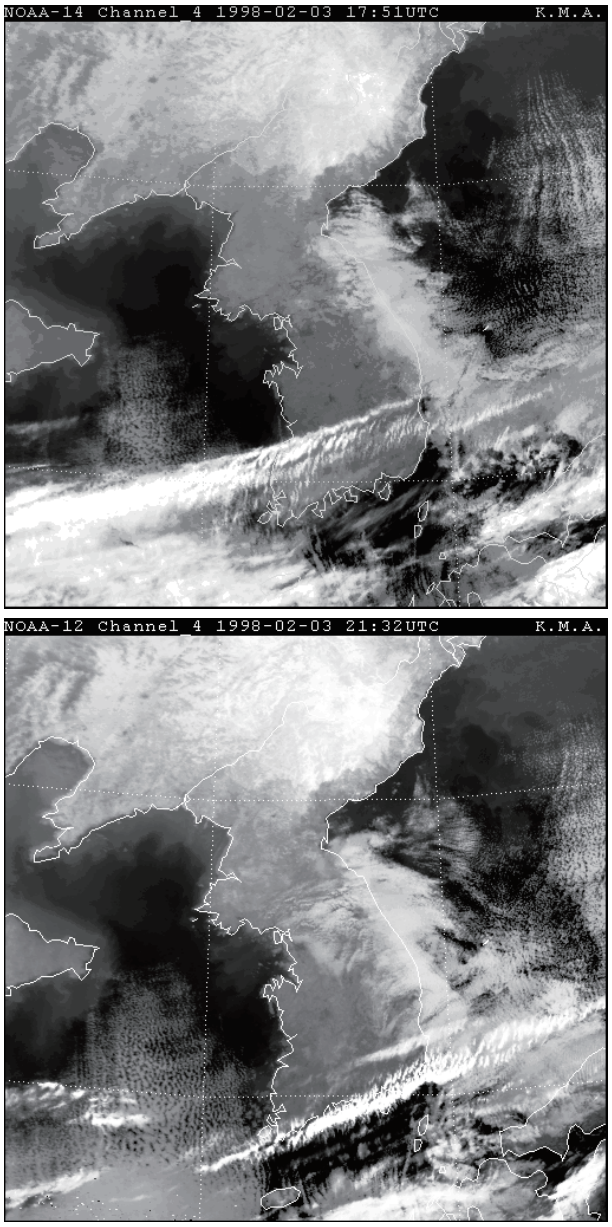

Fig. 3. The NOAA-12 Channel-4 satellite images at 1751 UTC 3 February (0251 LST 4 February, upper panel) and 2132 UTC 3 February (0652 LST 4 February) of 1998, lower panel), showing the active snowband along and off the eastern Korea coast.

resents a significant change in wind direction, from the northeasterly over the sea to the northwesterly over the land, as the air flow approached the coastal mountains. Such direction changes clearly indicate flow convergence in the coastal region. To better understand the more detailed flow structures and physical processes associated with this coastal snow fall event, we performed a set of numerical simulations, which will be discussed in the next section.

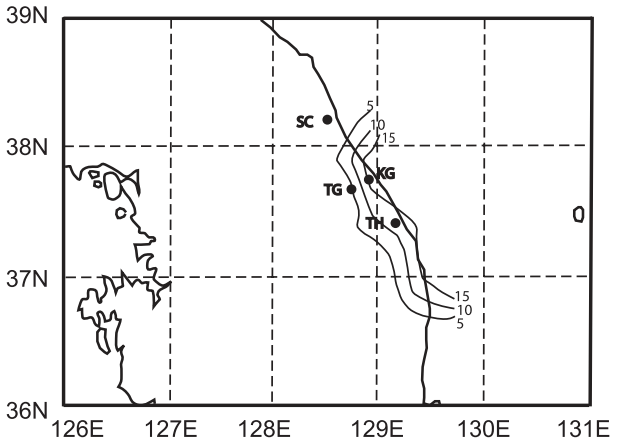

Fig. 4. Distribution of 24-h accumulated snowfall depth (5-cm contour intervals) ending at 1500 UTC 4 February 1998. SC, KG, TG and TH represent the locations of Sokcho, Kangnung, Taegwallyong and Tonghae, respectively.

3. Mdel description and numerical simulation

The numerical simulations used Version 5.0 of the Advanced Regional Prediction system (ARPS, Xue et al., 1995, 2000, 2001, 2003), a general-purpose, compressible, nonhydrostatic numerical weather prediction model. Several simulations were performed using different model start times and model resolutions, the start time of 1200 UTC 3 February was found to produce the best simulation results, which is a time of synoptic observations and is close to the beginning time of snowfall. Since the main goal of this study is to understand the fine-scale structure and physical processes associated with this event, we report only the results of the most successful simulation that started at 1200 UTC 3 February.

For this experiment, the computational grid consists of 179 points in both x and y directions with a horizontal resolution of 4 km (giving a physical domain of 704×704 km^2) and is centered at 39.3°N, 129.0°E (see Fig. 1). The vertically stretched grid consists of 43 levels, covering a depth of 17.2 km, with the vertical grid spacing varying from 20 m near the ground to about 800 m near the model top. The first model level is at about 10 m above ground and within the lowest 2-km depth there are 18 model layers. This vertical grid is believed to be adequate for resolving important vertical structures of the low-level phenomena including the cold-air damming and the frontal interface. The top and bottom model boundaries are rigid with a Rayleigh damping layer located above 12 km for controlling top-boundary wave reflection. The ice microphysics scheme of Lin et al. (1983) is used, which includes two liquid (cloud and rain) and three

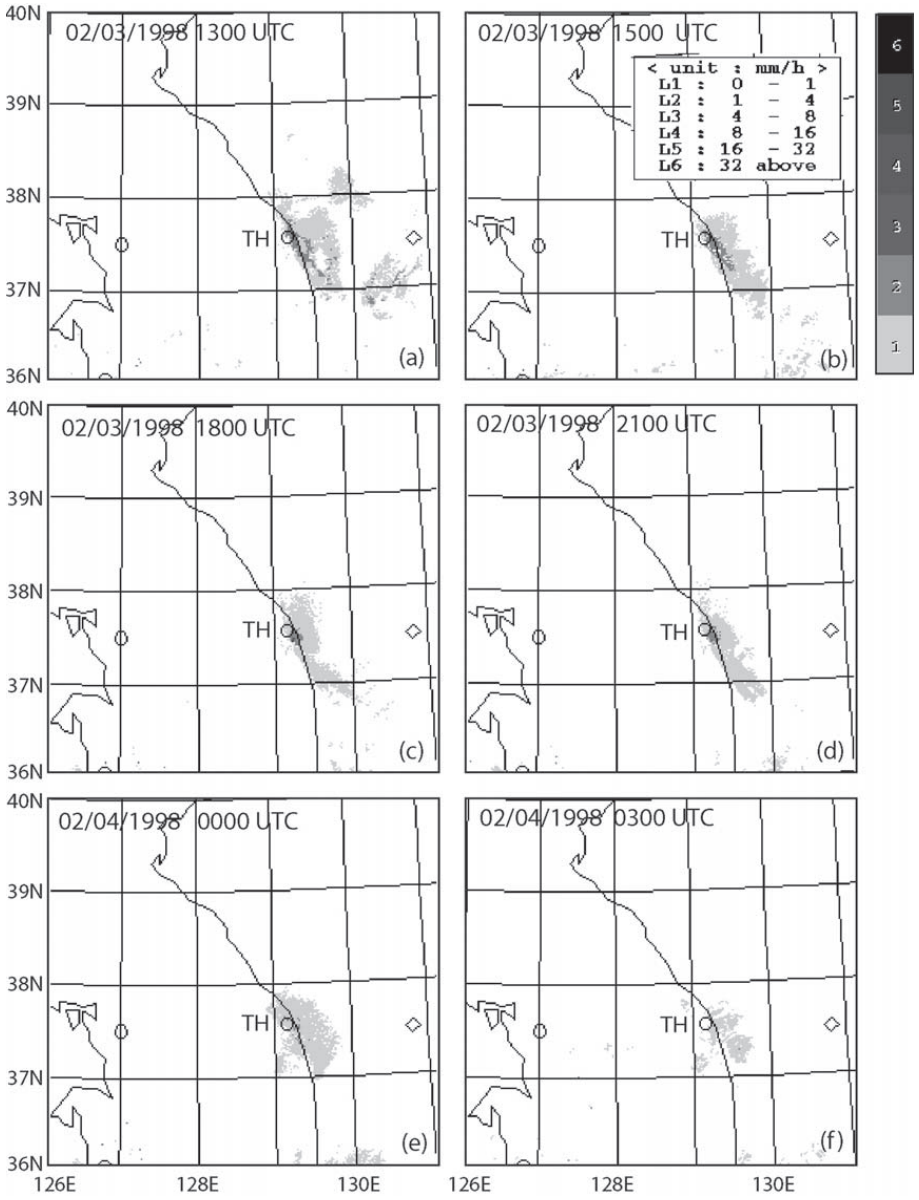

Fig. 5. Radar-derived precipitation rates based on observations of Tonghae radar (marked by the circle on the east coast and labeled TH) at the indicated times. Only the first two levels of precipitation rates (therefore levels of gray) are observed at all times shown.

ice categories (ice cloud, snow and hail or graupel). Subgrid-scale turbulent mixing is represented using an anisotropic 1.5-order turbulent kinetic energy closure scheme. The surface fluxes at the land surface are calculated using stability- and roughness-length-dependent drag coefficients, and the soil temperature and volumetric water content are predicted by a two-layer soil model. Meanwhile, the fluxes at the sea surface are calculated using drag and exchange coefficients that are appropriate for water surfaces under moderate-wind conditions, which are set to 2×10^{-3} following Chen et al. (1983). More details of the physics schemes in the ARPS can be found in Xue et al. (2001).

The soil model that predicts the soil skin temperature and soil moisture content is a two-layer force-restore model based on Noilhan and Planton (1989), where the offsets of top soil layer temperature and bottom soil layer from surface air temperature, as defined in Ren and Xue (2004), are set to be 1.0 K and 5.0 K, respectively, following the observations at sites in Yeongdong region. The terrain data used was

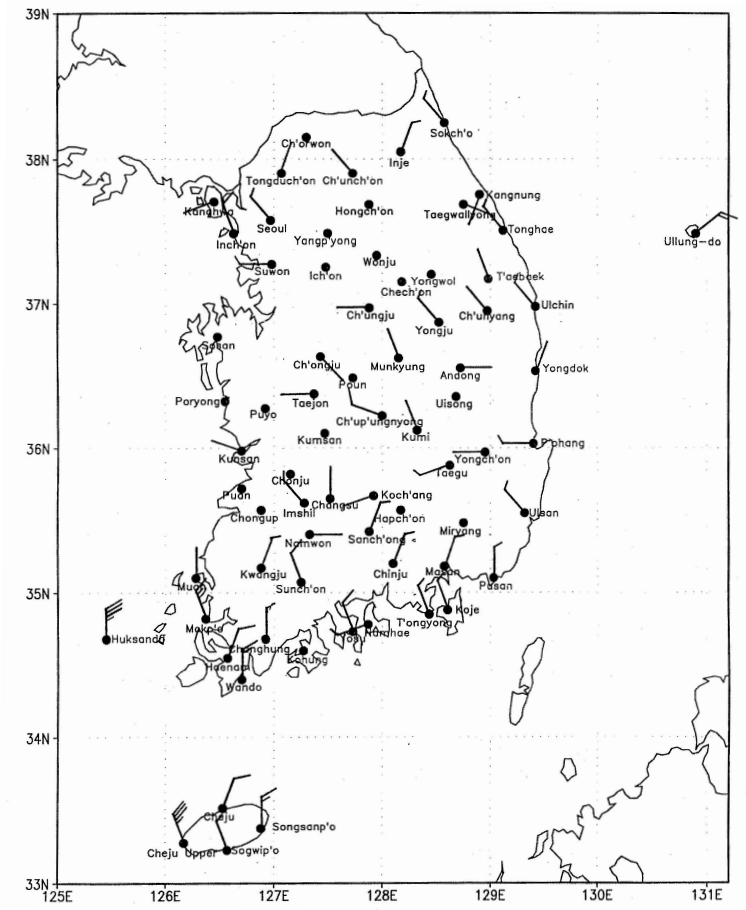

Fig. 6. Observed surface wind field at 1800 UTC 3 February 1998. One full barb represents 5 m s^{-1}.

derived from a 30-second terrain data base. Initial and boundary conditions came from the 40-km resolution RDAPS (Regional Data Assimilation and Prediction System of Korea Meteorological Administration, KMA, 1996). The ARPS was run for 24 hours, starting at 1200 UTC 3 February, about 1 hour before the onset of snowfall. Given the high grid resolution and the relatively narrow mountain range, the flow starting from the initial condition was able to rapidly respond to the fine-scale orography defined on our 4 km grid, although the 1200 UTC initiation time is probably somewhat too close to the onset time of snowfall to allow for sufficient spinup time. In the model, precipitation developed between 1300 and 1500 UTC, as will be discussed later.

4. Results of model simulation

As mentioned earlier, the ARPS model was run for a 24-h period starting at 1200 UTC 3 February 1998. Both observed and model simulated snow fall dissipated shortly after 0300 UTC 4 February. The precipitation system entered a mature stage after 1800 UTC and for several hours thereafter the coastal front and associated convergence zone remain quasi-stationary. We will first discuss the general evolution of the precipitation, then focus more on the flow and thermodynamic structures during the mature stage.

4.1 *Model simulated precipitation*

The model simulated precipitation rates at 1, 3, 6, 9, 12 and 15 hours of model time are shown in Fig. 7, together with the surface wind vector fields. During the first three hours (Figs. 7a and b), the surface winds over the ocean are mostly northerly, while those over land and near the coast are mostly northwesterly. By 1300 UTC (Fig. 7a), the model has not yet produced any precipitation near the coast even though at this time precipitation was already observed (Fig. 5a). The need for sufficient spinning up of precipitation from the 1200 UTC coarse-resolution RDAPS analysis is believed to be the main reason for such a delay.

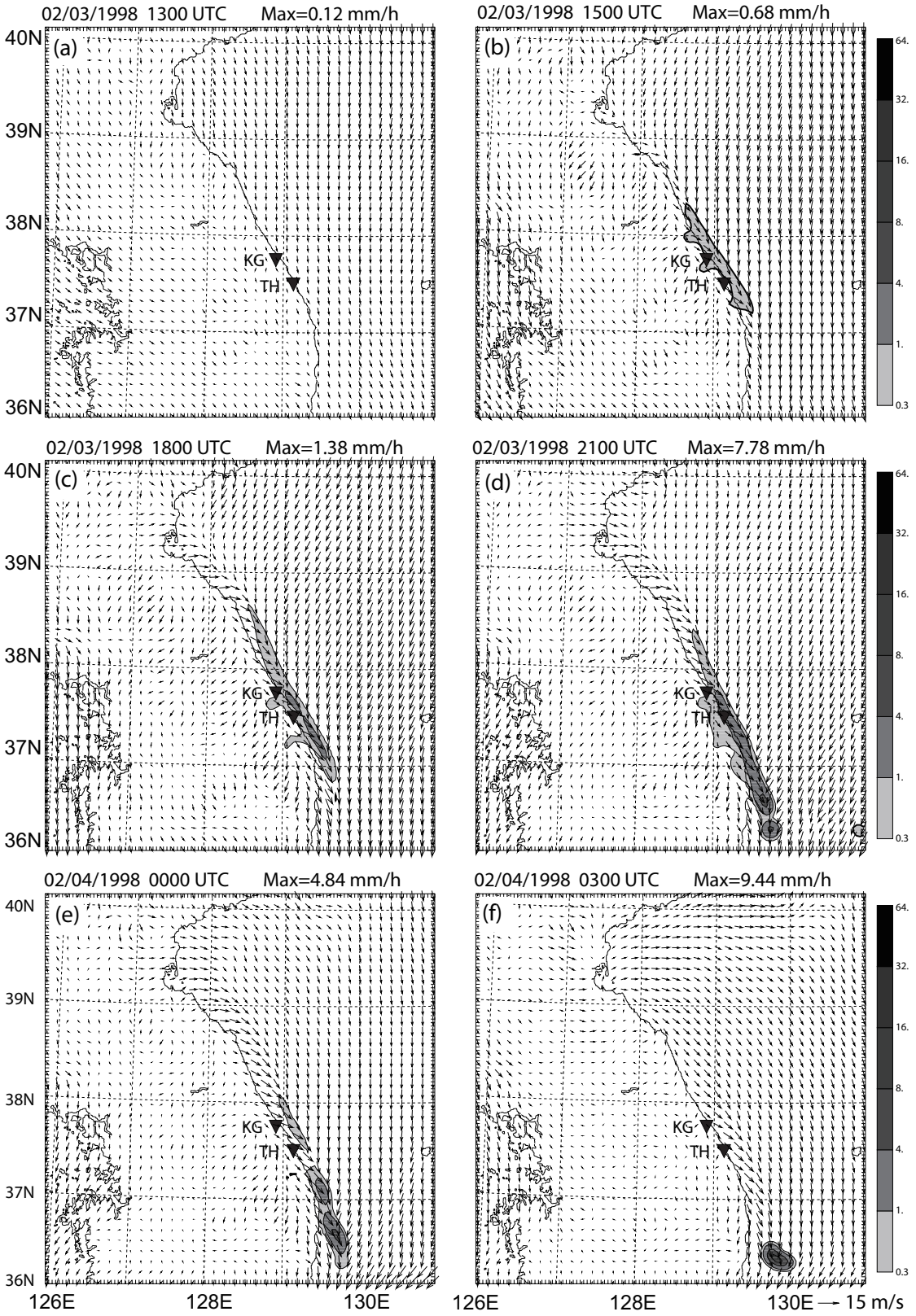

Fig. 7. Model simulated surface wind fields and the precipitation rates (shaded contours) corresponding to the radar-observed times in Fig. 5.

By 1500 UTC (Fig. 7b), the model has produced precipitation rates of up to 0.68 mm h^{-1}, along a narrow band near and off the east coast, close to Kangnung (KG) and Tonghae (TH). This agrees very well with the radar observation (Fig. 5b), except that the rates are somewhat under-predicted, which can at least be partially attributed to the delayed onset.

By 1800 UTC, or six hours into the simulation (Fig. 7c), the winds over the ocean have gained a significantly easterly component, which is consistent with the observation at the Ullung-do island shown in Fig. 6. Near the coast, the off-shore wind component has also become stronger (Fig. 7c), creating a strong surface convergence zone 10–15 km from the coast. Correspondingly, the strongest precipitation rates now exceed 1 mm h^{-1}, and the precipitation band is about twice as long as that at 1500 UTC. Radar estimated precipitation rates larger than 1 mm h^{-1} can also be found near Taewallyong at this time (Fig. 5c). Over the next three hours, the observed maximum precipitation rates remained more or less the same, while the region of light precipitation extended slightly south (Fig. 5d). In the model, the region with >1 mm h^{-1} precipitation is enlarged somewhat but remains generally along a narrow band near the coast. Precipitation rates of more than 4 mm h^{-1} are found at very small areas at and near the southern end of this precipitation band (Fig. 7d), which is more than the maximum observed. The development of a small region of strongest precipitation at this time and in the following 6 hours appears to be have been caused by some discontinuity near the southern model boundary (which is the southern boundary of the plotted domain in Fig. 7). If we choose to ignore such an anomaly (considering its proximity to the model boundary), the model simulated precipitation rates are generally below 4 mm h^{-1}, agreeing very well with the radar estimates.

At 2100 UTC, it is clear that the off-shore wind component is further enhanced, creating a somewhat stronger convergence zone, consistent with the enhanced precipitation. By 0000 UTC, the precipitation band is weakened, leaving only a small narrow band of precipitation of less than 1 mm h^{-1} near KG and TH (Fig. 7e). The same occurred in the radar observations. The length of observed precipitation band was shortened somewhat by this time, and precipitation rates exceeding 1 mm h^{-1} mostly disappeared (Fig. 5e).

The simulated precipitation along the coast completely disappeared by 0300 UTC, except for a small patch near the southern model boundary (Fig. 7f). In the radar observation, only very light precipitation remained at this time (Fig. 5f), and it disappeared completely by 0400 UTC (not shown). Clearly, the overall evolution, pattern as well as amount of simulated precipitation near the coast are very similar to those observed, suggesting the fidelity of the key physical processes simulated by the model.

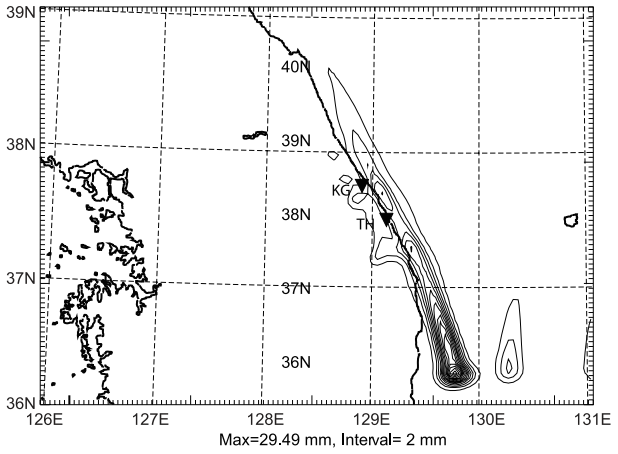

Fig. 8. Model simulated 24-hour accumulated precipitation (mm) ending at 1200 UTC 4 February 1998. Contour interval is 2 mm.

The 24-hour accumulated precipitation simulated by the model is shown in Fig. 8. It shows a maximum precipitation center at the southern end of the precipitation band, which we choose to discount because of the boundary-related discontinuity there. Along the coast near TH and KG, the simulated precipitation amount is 10–12 mm. Assume a density of fresh snow of 100 kg m^{-3}, or one tenth that of water, this gives a simulated snow depth of about 10–12 cm, which is close to the observed maximum of about 15 cm shown in Fig. 4. These results suggest that the mesoscale precipitation, in particular its spatial distribution, within this event is reproduced well by the model. The actual simulated precipitation amounts over land at Kangnung and Tonghae are lower than observed. The quantitative aspect of precipitation forecast is always a bigger challenge, and many aspects of the model, including the often insufficient resolution and inadequate model microphysics, can cause error in quantitative precipitation forecast. This can be a subject for future study.

4.2 *Model simulated flow and thermodynamic structures*

The 6-h simulated potential temperature θ, the equivalent potential temperature θ_e, water vapor mixing raito q_v, and the horizontal moisture convergence fields at the first model level or about 10 m above ground, valid at 1800 UTC 3 February 1998, are shown in Fig. 9, together with the horizontal winds at the

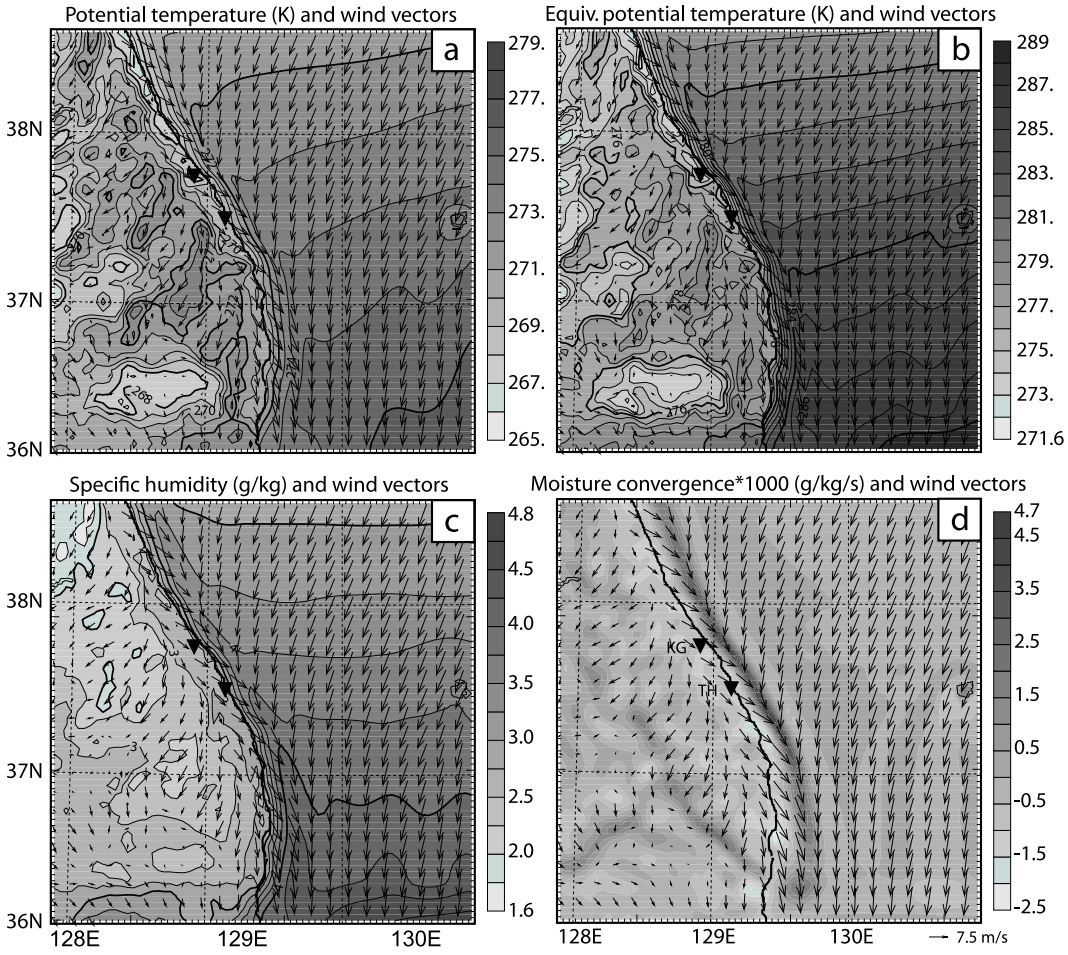

Fig. 9. The 6-hour model simulated surface winds and (a) potential temperature (K), (b) equivalent potential temperature (K), (c) specific humidity (g kg^{-1}), and (d) moisture convergence fields (1×10^{-3} g kg^{-1} s^{-1}), valid at 1800 UTC 3 February 1998.

same level. A very narrow wedge of cold air (thermal trough), as indicated by the lighter shading in the θ field (Fig. 9a), is found along the eastern slope of the Taebaek mountains and the coastal region; within this thermal trough are northerly winds that advect colder air from the north, all indicating the presence of cold-air damming. Meanwhile a broader thermal ridge just off the coast is quasi-parallel to the coast. Between the narrow thermal trough and the broad ridge are tightly packed θ contours corresponding to about 4-K difference over a distance of about 10 km, indicating the presence of a coastal mesoscale front. The θ_e field has an even stronger gradient along this front, with about 6-K difference across the front (Fig. 9b). This is due to the presence of strong moisture gradient also along the coast (Fig. 9c). Figure 9d shows clearly strong surface moisture convergence along the front. With the rich moisture supply from the ocean on the east side and the convergence lifting, the development of a precipitation band is not surprising.

Along line A-B in Fig. 1 that is roughly perpendicular to the mountain axis, vertical cross sections of temperature T, total water condensate mixing ratio and potential temperature θ, equivalent potential temperature θ_e and vertical velocity w, water vapor mixing ratio q_v, east-west wind component u, and the north-south wind component v are shown in Fig. 10 through Fig. 11 for 6 and 12 hours of model time, respectively. Also overlaid on these fields are the wind vectors projected to this cross section, except for the case of the north-south wind component v, where the horizontal wind barbs are shown.

A dome of cold air on the sea-facing mountain slope is indicated by the 272-K θ contour in the vertical cross-section, drawn as a thick dashed line in the figures. At six hours or 1800 UTC, the temperature of the cold dome ranges from 0°C on its eastern edge over the water and near the front to less than −6°C near the

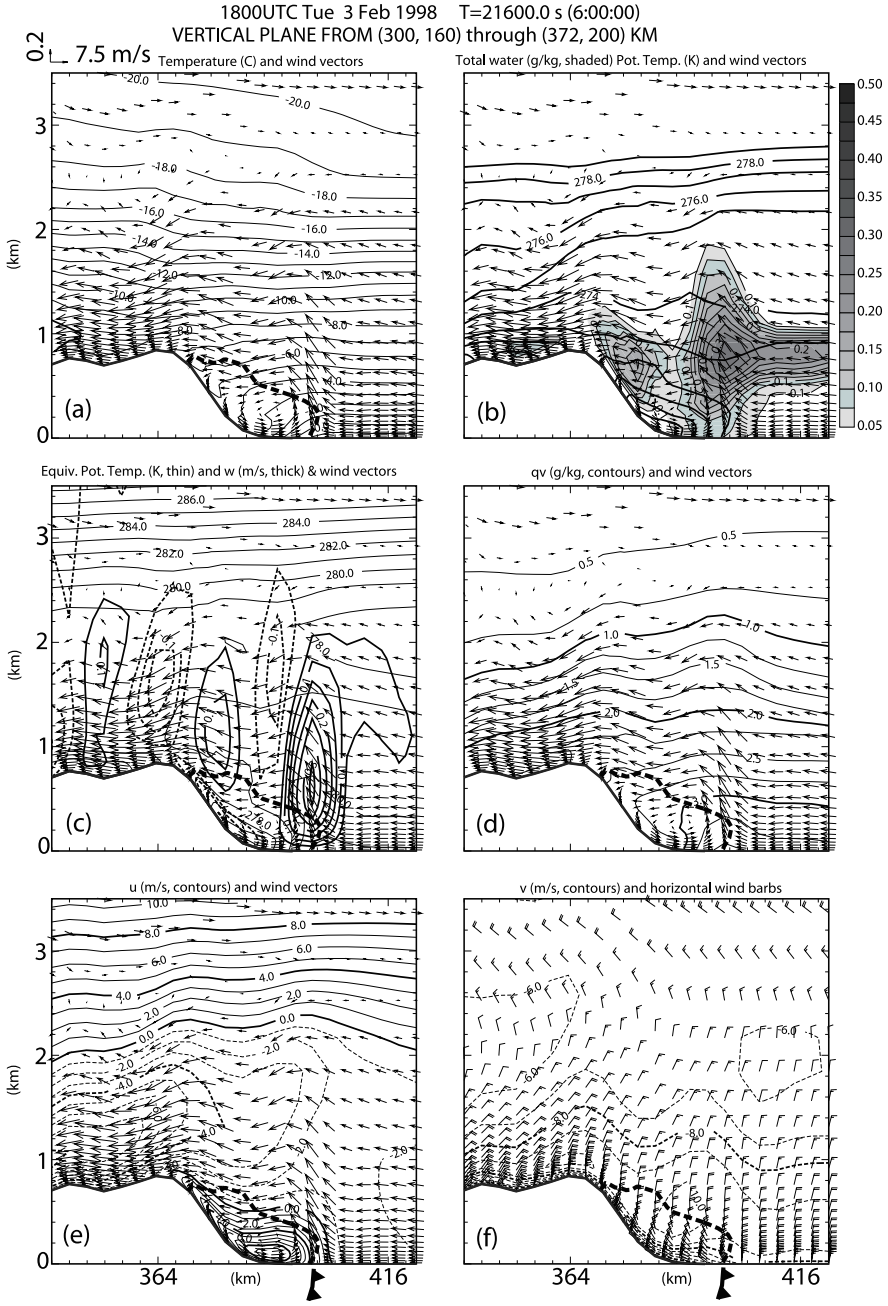

Fig. 10. Vertical cross-sections along line A-B in Fig. 1, of 6-hour model simulated (a) temperature (C°, contours), (b) total water condensate (g kg^{-1}, shaded contours) and potential temperature (K, thick contours), (c) equivalent potential temperature (K, thin contours) and vertical velocity w (m s^{-1}, thick contours), (d) specific humidity (g kg^{-1}), (e) east-west wind component u (m s^{-1}, contours), and (f) north-south wind component v (m s^{-1}, contours), at 1800 UTC 3 February 1998. The cross section roughly passes through Kangnung and is about perpendicular to the coastal mountain range. The horizontal axis labels represent the distances in km along the cross section. The wind vectors in (a) through (e) are wind vectors projected to the cross-section, and the wind barbs in (f) represent horizontal winds on the original model grid with one full barb representing 5 m s^{-1}. The dot line in (a) indicates the upper boundary of the frontal interface. Horizontal tick marks are 4 km apart.

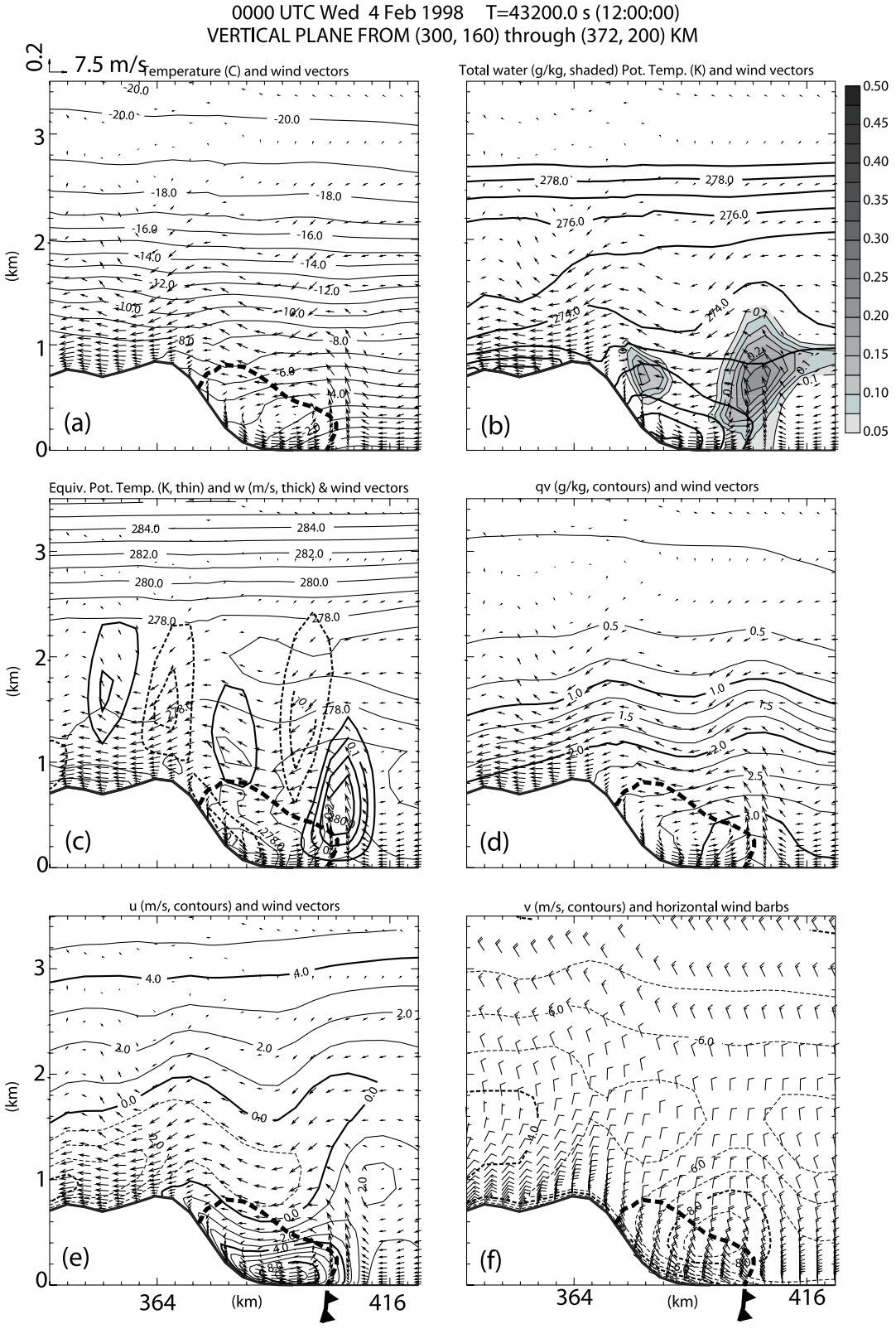

Fig. 11. Same as Fig. 10, but for 12 hours of model forecast valid at 0000 UTC 4 February 1998.

mountain top (Fig. 10a); inside the cold dome, the vertical stratification is roughly isothermal. Correspondingly, the θ field shows a strong static stability within the cold dome (Fig. 10b). Within the cold dome, there exists a rotor circulation in the cross section, with the surface flow running downslope towards the cold front, contributing to the convergence there. The downslope flow speed is as strong 9 m s^{-1} at this time (Fig. 10e). The horizontal wind barbs in Fig. 10f indicate northwesterly flows near the surface within the cold dome. The northerly wind component reaches 10 m s^{-1} at 500 m above sea level, indicating the presence of a low-level mountain-parallel jet. The jet core is roughly centered at the top of the cold dome and about half the mountain range peak height. The presence of the cold dome and low-level mountain-parallel jet is consistent with the phenomenon of cold-air damming. Stauffer and Warner (1987) carried out a numerical study to investigate the mesoscale structures associated with an Appalachian ice-storm case and showed a similar, low-level northerly jet east of the Appalachians. Because of the relatively coarse resolution used there (15 levels and 50 km horizontal grid spacing), the structures captured are of mesoscale or above while the Appalachian mountain range is also of a larger scale than the coastal mountain range considered here.

In our case, the damming occurs when the air flowing from the northeast as part of the Siberian High circulation is blocked at the low levels by the coastal mountains. As the air is slowed down, the Coriolis balance is disrupted, and the reduction of the Coriolis force associated with the reduced wind speed causes the air stream to turn leftward, in the down-gradient direction of the large-scale pressure gradient, creating a mountain-parallel low-level jet. This mountain-parallel flow advects cold air from the north, further decreasing the temperature of the dammed air (Bell and Bosart, 1988; Xu, 1990). In the sea-level pressure chart of the simulation (not shown), a wedge-shaped pressure ridge is evident along the eastern slopes of the mountains, which is the result of hydrostatic pressure effect of the dammed cold air and is found with typical cold-air damming cases.

Off the coast over the water, the near surface temperature is about 1°C, there is therefore about 4-K temperature difference over about 12 km, between the air over the ocean and the air at the mountain foot within the cold dome (Fig. 10a). Such a strong temperature gradient defines the coastal front. This temperature gradient is much stronger than the 10–15 K per 100 km gradient reported by Bosart (1981) based on buoy data for a case of coastal frontogenesis in the Carolinas of the United States, but is about half as large as the 5–10 K over 5–10 km across the New England coastal front studied in Bosart et al. (1972). The strength of such a coastal front can strongly depend on the background temperature gradient in the mountain parallel direction, and how long the mountain-parallel jet persists (e.g., Xu and Gao, 1995).

Being warmed by the surface heat fluxes over the ocean, the air in the lowest kilometer over the water is well mixed therefore nearly neutrally stratified (Fig. 10b). This air is also moist (given the air temperature), with a mixing ratio of close to 4 g kg^{-1} at the ocean surface (Fig. 10d). This incoming air is lifted at the front, producing an updraft maximum of about 1 m s^{-1} at about 600 m above sea level (Fig. 10c). This updraft is accompanied by condensation, giving rise of total water condensate of up to 0.4 g kg^{-1} that extends to about 2 km height (Fig. 10b). Some of the condensate reaches the ground in the form of precipitation. Because the precipitation falls behind (west of) the front within the sub-freezing air, it reaches the ground in the form of snow. The shallow depth of the updraft and clouds is mainly due to the presence of a layer of rather strong stability above the 2-km level. Below the 2-km level, because the low-level onshore flows originating from the well-mixed marine boundary layer does not contain much vertical shear, the updraft forced at the leading edge of the front tends to be tilted rearward (westward) instead of rising high due to baroclinic horizontal vorticity generation at the frontal zone (Rotunno et al., 1988), which is another factor favoring shallow convection.

The maritime air approaching the coastal mountain is lifted at the front and rises to produce condensational clouds and precipitation right behind the front (Fig. 10b). Located within the prevailing easterly flow below the 2.5-km level, much of this air continues to flow westwards after leaving the region of frontal updraft, and the flow at the low levels encounters mountain lifting near the top of the mountain range. This lifting produces a shallow layer of clouds near the mountain top, but no precipitation seems to be reaching the ground there (Fig. 10b).

Above the 2.5-km level, the environmental flow reverses from the easterly at the lower levels to westerly. Such flow reversal creates a critical level below which vertically propagating gravity waves are trapped. This is supported by the fact that the clear wave pattern found in the low-level w field ceases to exist about 2.6 km (Fig. 10c). Such trapped waves initially coming off the frontal region, being forced by the main convective updraft, can interact with the gravity waves forced by the mountain slope; based on the wavelength, the wave crest seems to be in phase with that forced by the mountain slope at this time (Fig. 10c), which would enhance the upward motion there. Even

so, no significant precipitation is found near the mountain top, which is believed to be due to the fact that the near-surface air on the mountain slope is too cold and dry. The presence of the surface downslope flow, which causes surface flow divergence near the mountain top also contributes negatively to precipitation development near the mountain top. The model simulated results clearly show that the displacement of the precipitation band away from the mountain slope to over the water is due to the cold-air damming over the eastern mountain slope and the establishment of a coastal front off the shore.

Over the next three hours until 2100 UTC, the general flow pattern in the vertical cross section did not change much. The coastal front remained essentially stationary while the frontal convection grew slightly deeper. The frontal updraft, cold dome depth and temperature, and the downslope flow all look very similar to those of 3 hours earlier (not shown). The horizontal cross section shows a slight southward shifting of the precipitation region during this period (Fig. 7).

At 0000 UTC the coastal front propagated eastward by about 4 km or one grid interval. The frontal cloud is now lower than 1.5 km and the precipitation reaching the ground has more or less disappeared (Fig. 11b, and also Fig 7e). The cold dome, as defined by the 272 K contour, is slightly deeper, and its internal rotor circulation is slightly stronger. The downslope flow speed maximum remains at about 9 m s^{-1} (Fig. 11e) although the maximum center is shifted away from the mountain foot. The most significant change is with the evident reduction in the speed of onshore flow ahead of the front (Fig. 11e), and this reduction is an indication of the start of the wind shift from northeasterly onshore flow towards the northwesterly flow associated with the synoptic-scale flow pattern change (Fig. 2). In fact, by this time, the horizontal winds at the A-B cross-section east of the front is mostly northerly (Fig. 11f), with a slight eastward component and with u showing small positive values (Fig. 11e) (note that the projection of the horizontal winds onto the west-southwest and east-northeast oriented A-B cross-section still shows onshore flow east of the front at this time). This wind shift removes the favorable cold-air damming condition. As the onshore flow weakens, the front and the cold air behind it move away from the mountain, losing the dammed air. The precipitation at the front therefore disappears over the next a few hours, as observed. Because of the strong temperature gradient therefore density gradient across the front, the dammed cold air can move away from the mountain like a density current when the onshore flow is taken away. Therefore, the coastal front of this study developed as the Siberian High expands toward the northern part of the East Sea, resulting in northeasterly onshore winds along the eastern coast of Korean Peninsula. The dissipation of the front occurs with the cession of the onshore winds when the Siberian High shrinks.

4.3 *Mountain blocking condition*

The effect of mountain blocking can be quantified by the Froude number, $Fr = U/(NH_{\rm m})$ (e.g., Forbes et al., 1987), where U is the speed of the component of the undisturbed wind normal to the mountain, and N is the Brunt-Väsälä frequency upstream of the mountain, and H_m is the mountain height, which is about 900 m in this study. The square of Fr is proportional to the ratio of the kinetic energy of the air to the amount of potential energy that has to be raised for the air parcel to reach the mountain top. The air can flow over the mountain without major deflection or blocking at a large enough Fr. At a low Fr, ranging from 0.5 to 2.3 (e.g., Kitabayashi, 1977; Mason and Skyes, 1978; Baines, 1979), the flow becomes blocked at low levels by the terrain. Forbes et al. (1987) also showed in their study of an Appalachian ice storm associated with the cold-air damming that at a small Fr (about 0.3 to 0.4), the flow was blocked and was flowing mainly in the mountain-parallel direction. In our case, the calculated Froude number is about 0.3 to 0.4 at the early and mature stages of cold-air damming. For example, at 1800 UTC or 6 h of simulation, the low-level inflow is about 2 m s^{-1} (Fig. 10e), the vertical difference in the inflow potential temperature in the depth of the mountain height is about 1 K (Fig. 10e). This gives rise to $Fr \approx 0.35$, therefore the blocking effect of the terrain is dominant. The air flows are decelerated (instead of running up the mountain slope) and then turned leftward to become parallel to the mountains, driven by the large-scale pressure gradient force in the mountain parallel direction (Xu, 1990).

5. Summary and conclusions

The processes and mechanisms of a heavy snowfall event that occurred in the Yeongdong coastal region of the Korean Peninsula are studied using observational data and through a high-resolution model simulation. The numerical simulation using a 4-km horizontal resolution and 43 vertically-stretched levels reproduces very well the narrow snowband located off the eastern Korean coast, away from instead of over the coastal mountain range. The general evolution of the snowband agrees quite well with the radar observations, while the precipitation amount agrees reasonably well with the radar estimate. The simulation results clearly

show that this precipitation band developed due to the forcing of a coastal front which developed because of the damming of cold air against the eastern slope of the coastal mountain range. The dammed cold air was enhanced by the advection of cold air by a mountain-parallel jet, which formed due to geostrophic adjustment as previously published theory suggested, when the on-shore upslope air was decelerated by the mountain blocking.

While the cold-air damming and associated precipitation processes have been studied at other parts of the world and in particular in the eastern coastal region of the United States in connection with the larger Appalachian mountain range, detailed studies on such events in the Korean region have not been done until very recently. Furthermore, the coastal mountain ranges and the associated features of cold-air damming and coastal front are of much smaller scales in the Korean region than most of those that occur east of the Appalachian mountain; the latter have received most attention in the literature. Earlier studies, due to their use of much coarser resolution data and model, focus more on the synoptic scale and mesoscale, instead of the mesoscale to small scale. In this study, high-resolution high-frequency radar observations are used to verify the model simulation to better establish the credibility of modeling results. The synoptic settings as well as their evolution studied here also differ from the typical situations in eastern United States. In this case, the presence and migration of the Siberian High played an important role in the establishment and dismantling of cold-air damming. Specific evolution from the initial to decaying stage of the particular snow event studied in this paper is summarized as follows:

(1) With the expansion of the Siberian High, cold air outbreak occurred over the northern part of the East Sea. This provided the initial trigger for the heavy snowfall near the coast. The cold air, being on the east side of the High, was advected southwestward over the warm sea surface, collecting a large amount of heat and moisture. Scattered clouds formed over the sea.

(2) Cold air flowing onshore, from the northeast after a long fetch over the warm water, was dammed against the eastern slope of the mountain range that is parallel to the coast, due to the blocking effect of the mountain barrier. The decelerated flow turned leftward due to geostrophic adjustment, establishing a northerly mountain-parallel jet that advects cold air from the north and enhancing the cold-air damming.

(3) The dense cold air accumulating on the eastern slope of the mountain range attempted to move downslope towards the sea, enhancing the convergence and temperature gradient along a coastal front that was established as a result.

(4) The development and organization of a cloud band along the coastal front led to the heavy snowfall along the coast, with its maximum located about 10 km off the coast. The cold-air damming and the formation of the coastal front explain why the heaviest snowfall was not found over the mountain slope, where the orographic lifting is the strongest.

(5) A synoptic-scale pressure pattern change, which in this case was the retreat of the Siberian High away from the northern East Sea, led to the shift in the wind direction from north-northeasterly to northwesterly in the coastal region and off coast at later times. This resulted in the weakening of convergence and temperature gradient across the front and the seaward propagation and eventual dissipation of the front. The associated precipitation also ceased afterwards.

Due to the lack of detailed *in-situ* data over the ocean, we were unable to verify some of the fine-scale details of our simulation. When data are available, including high-frequency radar observations, the agreement between the model and observations is rather good, lending creditability to the simulation results. Many of the simulated meso-β and meso-γ scale features associated with the sequence of events described here are physically consistent. By analyzing the model output, a much better understanding of the location, structure and formation mechanism of the precipitation has been gained for the specific geographic region studied. The general understanding should also apply to similar events occurring at other parts of the world that have similar geographic and synoptic situations. Compared to earlier numerical studies of cold-air damming events, a much higher model resolution is used here, which is necessary to resolve the smaller scale geographical as well as atmospheric features that seem to be typical of this particular geographical region. The numerical simulation did under-predict the amount of precipitation somewhat; model resolution, physics, as well as initial condition deficiencies can all contribute to such quantitative errors. Accurate quantitative precipitation forecast is not the central focus of this paper but can be investigated in future studies. Finally, we point out that another similar case that occurred in the Yeongdong region had been studied by Lee and Kim (2008) and Lee et al. (2011) and the results of the current study are consistent with theirs.

Acknowledgements. This work was primarily supported by the National Research Foundation of Korea (NRF) grant funded by the Korea government (MEST) (Grant No. 2011-0013879). Ming XUE was supported by NSF (Grant Nos. AGS-0802888, AGS-1046171, and EEC-0313747).

REFERENCES

Atlas, D., S-H. Chou, and W. P. Byerly, 1983: The influence of coastal shape on winter meso-scale air-sea interaction. *Mon. Wea. Rev.*, **111**, 245–252.

Baines, P. G., 1979: Observations of stratified flow past three-dimensional barriers. *J. Geophys. Res.*, **84**, 7834–7838.

Bell, D. G., and L. F. Bosart, 1988: Appalachian cold-air damming. *Mon. Wea. Rev.*, **116**, 137–162.

Bosart, L. F., 1975: New England coastal frontogenesis. *Quart. J. Roy. Meteor. Soc.*, **101**, 957–978.

Bosart, L. F., 1981: The President's Day snowstorm of 18-19 February 1979: A subsynoptic-scale event. *Mon. Wea. Rev.*, **109**, 1542–1566.

Bosart, L. F., D. J. Vaudo, and J. H. Heldson Jr., 1972: Coastal frontogenesis. *J. Appl. Meteor.*, **11,** 1236–1258.

Chen, T. C., C. B. Chang, and D. J. Perkey, 1983: Numerical study of an AMTEX 75 oceanic cyclone. *Mon. Wea. Rev.*, **111**, 1818–1829.

Eichenlaub, V. L., 1979: *Weather and Climate of the Great Lakes Region.* University of Notre Dame Press, 335pp.

Estoque, M. A., and K. Ninomiya, 1976: Numerical simulation of Japan Sea effect snowfall. *Tellus*, **28**, 243–253.

Forbes, G. S., R. A. Anthes, and D. W. Thomson, 1987: Synoptic and mesoscale aspects of an Appalachian ice storm associated with cold-air damming. *Mon. Wea. Rev.*, **115**, 564–591.

Hjelmfelt, M. R., and R. R. Braham Jr., 1983: Numerical simulation of the air flow over Lake Michigan for a major lake-effect snow event. *Mon. Wea. Rev.*, **111**, 205–219.

Jhun, J.-G, D.-K. Lee, and H.-A. Lee, 1994: A study on the heavy snowfalls occurred in South Korea. *J. Korean Meteor. Soc.*, **30**, 97–117. (in Korean with English abstract)

Kitabayshi, K., 1977: Wind tunnel and field studies of stagnant flow upstream of a ridge. *J. Meteor. Soc. Japan*, **55**, 193–203.

KMA, 1996: A new numerical weather prediction system at KMA. Technical Report 96-2, 147pp. (in Korean)

Lee, H., and T.-Y. Lee, 1994: The governing factors for heavy snowfalls in Youngdong area. *J. Korean Meteor. Soc.*, **30**, 197–218. (in Korean with English abstract)

Lee, J. G., 1999: Synoptic structure causing the difference in observed snowfall amount at Taegwallyong and Kangnung. *Asia-Pacific Journal of Atmospheric Sciences*, **35**, 319–334. (in Korean with English abstract)

Lee, J. G., and Y. J. Kim, 2008: A numerical simulation study using WRF of a heavy snowfall event in the Yeongdong coastal area in relation to the northeasterly. *Atmosphere*, **18**, 339–354. (in Korean with English abstract)

Lee, J. G., S.-D. Kim, and Y.-J. Kim, 2011: A trajectory study on the heavy snowfall phenomenon in Yeongdong region of Korea. *Asia-Pacific Journal of Atmospheric Sciences*, **47**, 45–62.

Lin, Y.-L., R. D. Farley, and H. D. Orville, 1983: Bulk parameterization of the snow field in a cloud model. *J. Climate Appl. Meteor.*, **22**, 1065–1092.

Mason, P. J., and R. I. Skyes, 1978: On the interaction of topography and Ekman boundary layer pumping in a stratified atmosphere. *Quart. J. Roy. Meteor. Soc.*, **104**, 475–490.

Nagata, M., M. Ikawa, S. Yoshizumi, and T. Yoshida, 1986: On the formation of a convergent cloud band over the Japan sea in winter: Numerical experiments. *J. Meteor. Soc. Japan,* **64**, 841–855.

Ninomiya, K., 1968: Heat and water budget over the Japan sea and the Japan islands in winter season. *J. Meteor. Soc. Japan*, **46**, 343–372.

Niziol, T. A., W. R. Snyder, and J. S. Waldstreicher, 1995: Winter weather forecasting throughout the eastern United States. Part IV: Lake effect snow. *Wea. Forecasting*, **10**, 61–77.

Noilhan, J., and S. Planton, 1989: A simple parameterization of land surface processes for meteorological models. *Mon. Wea. Rev.*, **117**, 536–549.

Ren, D., and M. Xue, 2004: A revised force-restore model for land-surface modeling. *J. Appl. Meteor.*, **43**, 1768–1782.

Richwien, B. A., 1980: The damming effect of the southern Appalachians. *Natl. Wea. Dig.*, **5**, 2–12.

Rotunno, R., J. B. Klemp, and M. L. Weisman, 1988: A theory for strong long-lived squall lines. *J. Atmos. Sci.*, **45**, 463–485.

Sanders, F., and J. R. Gyakum, 1980: Synoptic dynamic climatology of the bomb. *Mon. Wea. Rev.*, **108**, 1589–1606.

Seo, E.-K., and J.-G. Jhun, 1991: A case study of the heavy snowfalls occurred in the Korean peninsula from 29 January to 1 February 1990. *J. Korean Meteor. Soc.*, **27**, 165–179. (in Korean with English abstract)

Skamarock, W. C., J. B. Klemp, J. Dudhia, D. O. Gill, D. M. Barker, W. Wang, and J. D. Powers, 2005: A Description of the advanced research WRF version 2, NCAR Tech. Note NCAR/TN-468+STR, 88pp.

Stauffer, D. R., and T. T. Warner, 1987: A numerical study of Appalachian cold-air damming and coastal frontogenesis. *Mon. Wea. Rev.*, **115**, 799–821.

Waldstreicher, J. S., 2002: A foot of snow from a 3000-foot cloud-The ocean-effect snowstorm of 14 January 1999. *Bull. Amer. Meteor. Soc.*, **83**, 19–22.

Xu, Q., 1990: A theoretical study of cold-air damming. *J. Atmos. Sci.*, **47**, 2969–2985.

Xu, Q., and S. Gao, 1995: An analytic model of cold air damming and its applications. *J. Atmos. Sci.*, **52**, 353–366.

Xue, M., K. K. Droegemeier, V. Wong, A. Shapiro, and K. Brewster, 1995: ARPS Version 4.0 User's Guide. [Available online at http://www.caps.ou.edu/ARPS.]

Xue, M., K. K. Droegemeier, and V. Wong, 2000: The Advanced Regional Prediction System (ARPS)—A multiscale nonhydrostatic atmospheric simulation and prediction tool. Part I: Model dynamics and verification. *Meteor. Atmos. Phys.*, **75**, 161–193.

Xue, M., and Coauthors, 2001: The Advanced Regional Prediction System (ARPS)—A multi-scale nonhydrostatic atmospheric simulation and prediction tool. Part II: Model physics and applications. *Meteor. Atmos. Phys.*, **76**, 143–166.

Xue, M., D.-H. Wang, J.-D. Gao, K. Brewster, and K. K. Droegemeier, 2003: The Advanced Regional Prediction System (ARPS), storm-scale numerical weather prediction and data assimilation. *Meteor. Atmos. Phys.*, **82**, 139–170.